

Constructing Physics-Based Facial Models of Individuals

Yuencheng Lee¹, Demetri Terzopoulos^{1,3}, and Keith Waters²

¹Department of Computer Science, University of Toronto, Toronto, ON, M5S 1A4

²Digital Equipment Corporation, Cambridge Research Lab, One Kendall Square, Cambridge, MA 02139

Abstract

This paper develops a highly automated approach to constructing realistic, working models of human heads for use in animation. These physics-based models are anatomically accurate and may be made to conform closely to specific individuals. We begin by scanning a person with a laser sensor which circles around the head, acquiring detailed range and reflectance information. Next, an automatic conformation algorithm adapts a triangulated face mesh of predetermined topological structure to these data. The generic mesh, which is reusable with different individuals, reduces the range data to an efficient, polygonal approximation of the facial geometry and supports a high-resolution texture mapping of the skin reflectivity. The conformed polygonal mesh forms the epidermal layer of a new, physics-based model of facial tissue. An automatic algorithm constructs the multilayer synthetic skin and estimates an underlying rigid "skull" substructure with a jointed jaw. Finally, the algorithm inserts synthetic muscles into the deepest layer of the facial tissue. These contractile actuators, which emulate the primary muscles of facial expression, generate forces that deform the synthetic tissue into meaningful expressions. To increase realism, we include constraints to emulate tissue incompressibility and to enable the tissue to slide over the skull substructure without penetrating into it. The resulting animate models appear significantly more realistic than our previous physics-based facial models.

Keywords: *Physics-Based Facial Modeling, Facial Animation, Cylindrical Facial Scanning, Feature-Based Facial Adaptation, Texture Mapping, Discrete Deformable Models.*

1 Introduction

The human face has fascinated computer graphics modelers since the early 1970's. An important research goal has been to improve the realism of facial models. Over the years, researchers have progressed from simple, polygonal facial meshes, to parameterized models, to state-of-the-art physical models, each evolutionary step assimilating the best features of the previous generation of facial modeling methods [6].

We have developed a physics-based approach to modeling the human face which pays serious attention to its anatomical structure and elaborate biomechanics [8, 12]. Starting from conventional facial meshes, our models incorporate a synthetic facial tissue (a dynamic, multilayer spring-mass lattice with nonlinear elastic properties) and anatomically

well-positioned synthetic muscles (a modification of the earlier parameterized muscle process of [10]).

Traditionally, facial meshes have been constructed manually from two or more views of the face or by manually digitizing plaster casts. This laborious and error prone task has been superseded by active laser scanners [1, 4]. Scanners, such as the one manufactured by Cyberware, Inc., circles around a person's head to acquire high resolution, regularly sampled range and reflectance information. To take advantage of these scanners in human facial modeling and animation, our goal is to develop efficient and highly automated methods for constructing working facial models of individuals from the acquired data [11].

In this paper we consider the problem of individualizing physics-based facial models. In particular we develop a predominantly automatic method for constructing realistic, working models of individual's heads for use in animation. The method begins with detailed radial range and reflectance images acquired from an individual using the Cyberware scanner [1].

We develop an automatic conformation algorithm which adapts a triangulated face mesh of predetermined topological structure to the scanned data. This generic mesh, which is reusable with different individuals, is designed to reduce the range data to an efficient, polygonal approximation of the facial geometry and to support a high-resolution texture mapping of the skin reflectivity. The generic mesh is adapted through a search for salient local minima and maxima of a scalar field function of the range image. The search is directed according to the known relative positions of nose, eyes, chin, ears, and other facial features with respect to the generic mesh. Facial muscle emergence and attachment points are known relative to the generic mesh, and their positions are adapted as the mesh is conformed to the data.

The conformed facial mesh forms the epidermal layer of a new, physics-based model of facial tissue, a variant of the model in [8, 12]. This synthetic tissue is a dynamic spring-mass lattice composed of triangular prism elements with internal constraints that emulate tissue incompressibility. An automatic algorithm constructs the multilayer synthetic skin and it also estimates an underlying "skull" structure with a jointed jaw. Finally, the algorithm inserts synthetic muscles into the deepest, muscle layer of the tissue. These contractile actuators, which emulate the primary muscles of facial expression, generate forces that deform the synthetic tissue into meaningful expressions. To increase realism, we include new constraints that enable the deforming facial tissue to slide over an estimated skull structure without penetrating into it as the muscles contract and as the jaw opens.

³Fellow, Canadian Institute for Advanced Research
E-mail addresses: {vlee | dt}@vis.toronto.edu, waters@crl.dec.com



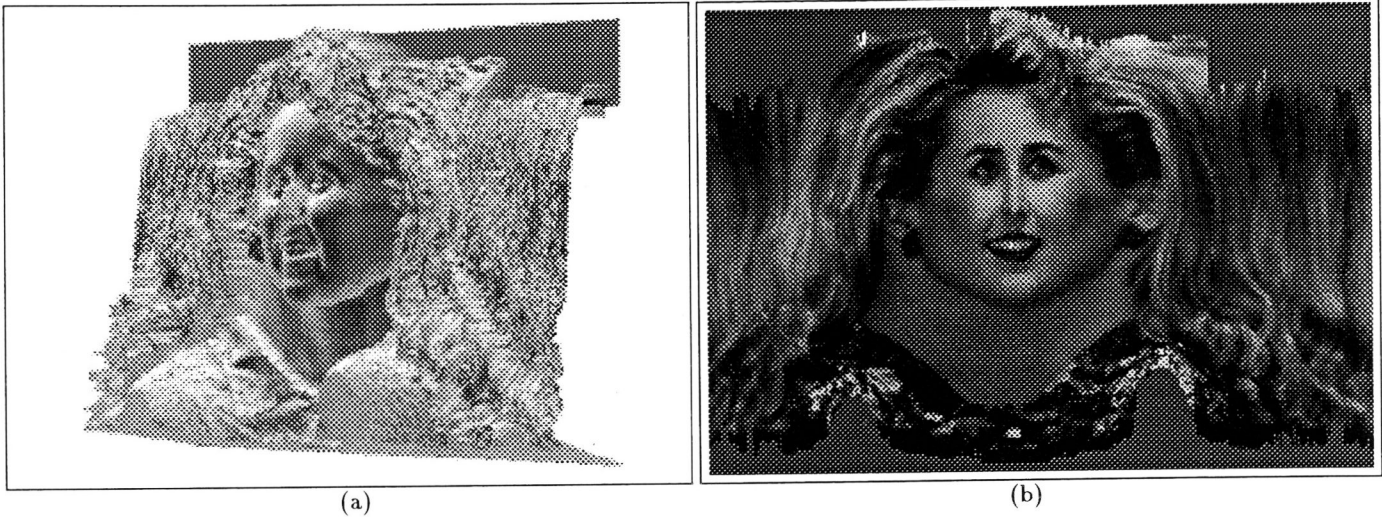


Figure 1: "Heidi" data from Cyberware, Inc. (a) 3D display of range data magnitude. (b) RGB texture map.

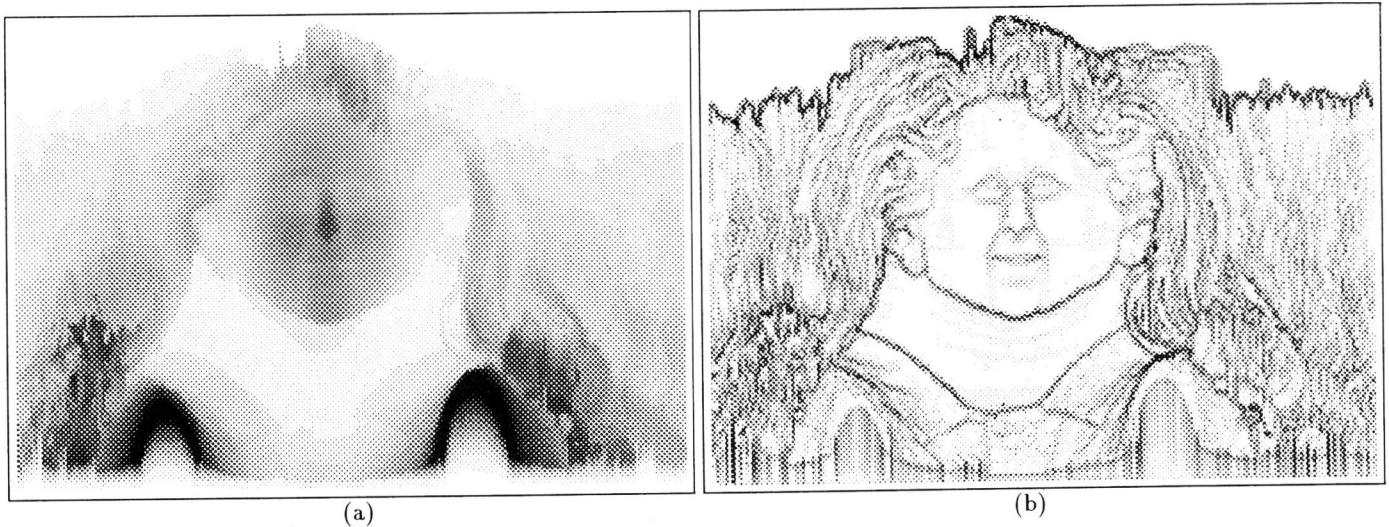


Figure 2: Range image (a) and positive Laplacian of range magnitude (b).

2 Cylindrical Laser Range Data

The typical output of the Cyberware color 3D scanner consists of 512×256 range and reflectance (RGB) values. Each range value represents the distance from the source to the object in cylindrical coordinates with corresponding longitude (0–360 degrees) and latitude. The range data from Cyberware's "Heidi" data set are displayed as a three dimensional range surface in Fig. 1(a) and as a two dimensional image Fig. 2(a) with intensity representing range. Fig. 1(b) shows the RGB texture map as a monochrome image.

Although the head structure in the cylindrical laser range data is distorted along the longitudinal direction, important features such as the slope changes of the nose, forehead, chin, and the contours of the mouth, eyes, and nose are still discernible. These facial features become more evident after applying a modified Laplacian operator to the range map $r_{i,j}$ shown in Fig. 2(a) to produce the field function $l_{i,j}$ in Fig. 2(b). The operator is approximated by the following

finite difference formulas:

$$\begin{aligned} l_{i,j}^x &= P(r_{i-1,j} - 2r_{i,j} + r_{i+1,j})/h^2 \\ l_{i,j}^y &= P(r_{i,j-1} - 2r_{i,j} + r_{i,j+1})/h^2 \\ l_{i,j} &= l_{i,j}^x + l_{i,j}^y \end{aligned}$$

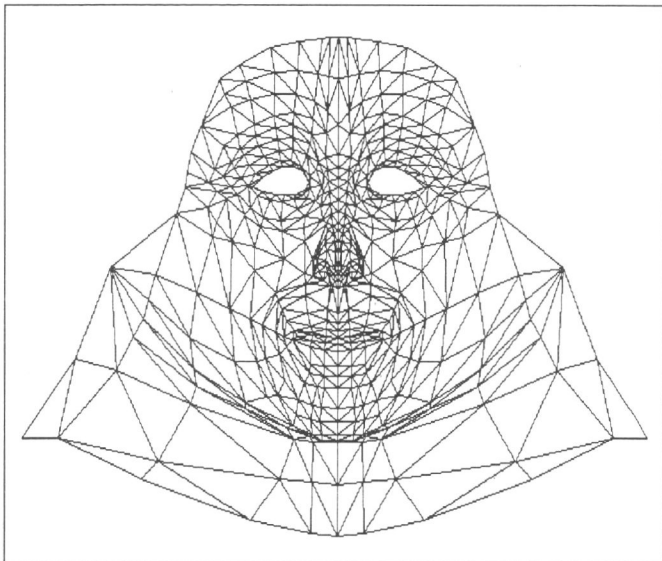
where l^x, l^y are the positive second derivatives of depth in the x, y directions, $h = 1$ is the discrete step size, and

$$P(x) = \begin{cases} x & \text{if } x > 0 \\ 0 & \text{otherwise.} \end{cases}$$

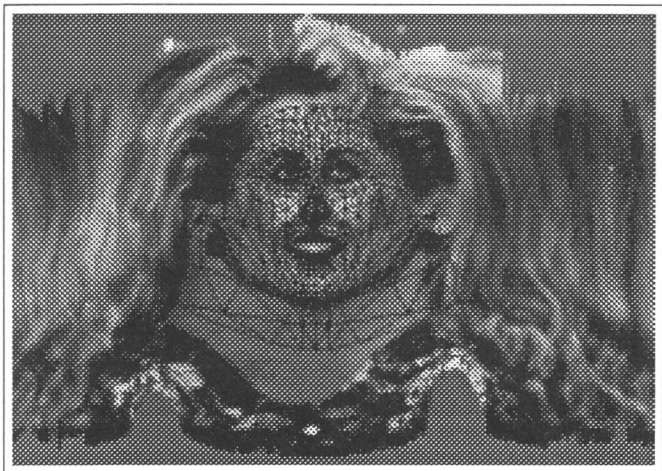
3 Generic Face Mesh and Mesh Adaptation

Motivated by the "adaptive mesh" developed in [7] and employed in [11], we have developed a different approach to adapting the face model to the scanned data by deforming an irregularly triangulated generic face mesh. Fig. 3(a) shows the planar generic mesh which we obtain through a cylindrical projection of the 3D face mesh from [10] (see Fig. 4(a)). Among the advantages of the generic mesh is that its irregularly triangulated structure reduces the number of degrees

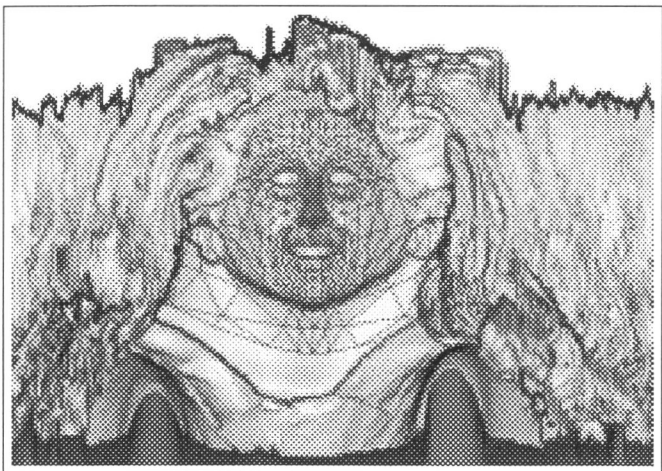




(a)



(b)



(c)

Figure 3: Adapting the generic face mesh. (a) Unadapted generic mesh. (b) Adapted mesh superimposed on the texture map. (c) Adapted mesh superimposed on a gradient map.

of freedom in the final face model and it has well defined features which form the basis for accurate adaptation and positioning of facial muscles.

We label all facial feature nodes in the generic face (Fig. 4(a)) prior to the adaptation step. Feature nodes include eye contours, nose contours, mouth contours, and chin contours.

For any specific range image and its positive Laplacian field function (e.g., Fig. 2), the generic mesh adaptation procedure performs the following steps to locate feature points in the range data:

1. Locate the highest range data point in the central area, and globally translate the face mesh to achieve correspondence with the tip of the nose.
2. Locate the chin as the point below the nose with the greatest value of the positive Laplacian of range.
3. Locate the mouth as the point of greatest positive Laplacian between the nose and chin, and scale the positions of all mesh nodes below the nose accordingly.
4. Locate the chin contour as the points whose latitudes lie in between the mouth and chin, and scale all mesh nodes below the chin contour.
5. Locate the ears as the points with a positive Laplacian larger than a threshold value around the longitudinal direction of the nose, and scale all the mesh nodes horizontally.
6. Locate the eyes as the points which have the greatest positive Laplacian around the estimated eyes region, and scale all the mesh nodes above the nose.
7. To fine-tune the mesh nodes after the above adaptation steps, activate spring forces in the planar mesh with the adapted feature nodes treated as immobile boundary conditions (see [7]). As the springs attempt to minimize their deformations, the node positions between features will become regularized according to their original distances in the generic mesh. Fig. 3(b-c) shows the results of mesh adaptation.
8. Extend the generic mesh geometrically over the rest of the range data to cover the hair.
9. Conform the adapted generic mesh to the 3D geometry and reflectance of the scanned individual by storing the adapted 2D nodal positions as RGB texture map coordinates and by sampling the radial range image at 2D nodal positions to compute the 3D positions of the mesh nodes (Fig. 4(b-c)).

The above automatic, multistep adaptation algorithm gives satisfactory results with the relatively clean "Heidi" data set. We have also applied it to more difficult data sets acquired from subjects with nonsalient facial features and/or under unfavorable lighting conditions. In such cases it becomes necessary to adjust the positions of some adapted mesh nodes around important facial features such as the eyes, mouth, and chin. We can typically make the necessary manual adjustments in about 15 minutes.



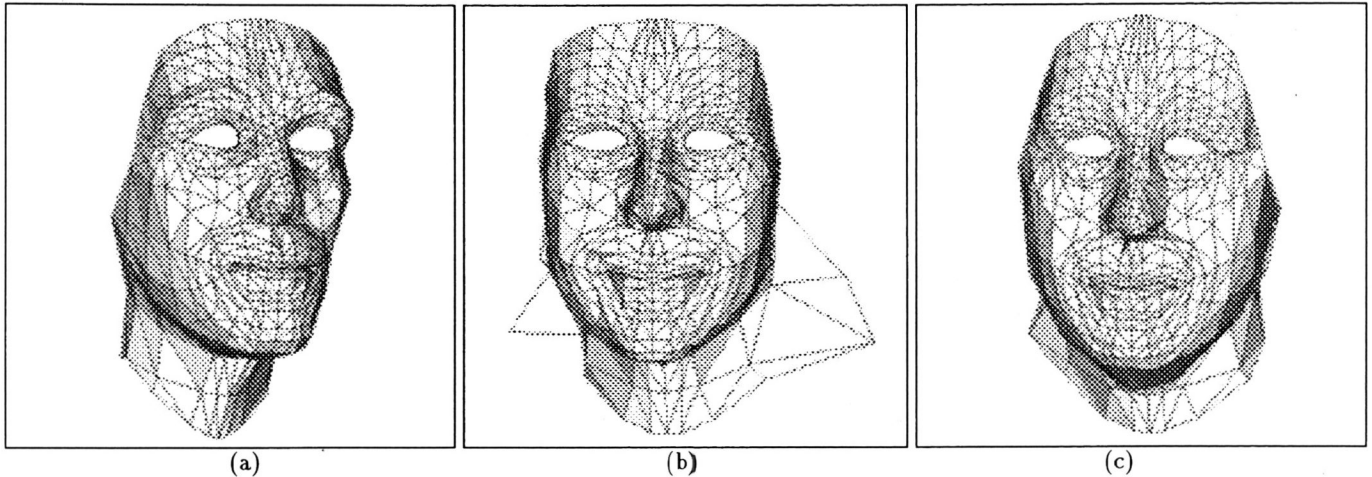


Figure 4: Conforming the generic face mesh to several face geometries Generic mesh (a). Generic mesh conformed to “Heidi” data (b). Generic mesh conformed to another data set (c).

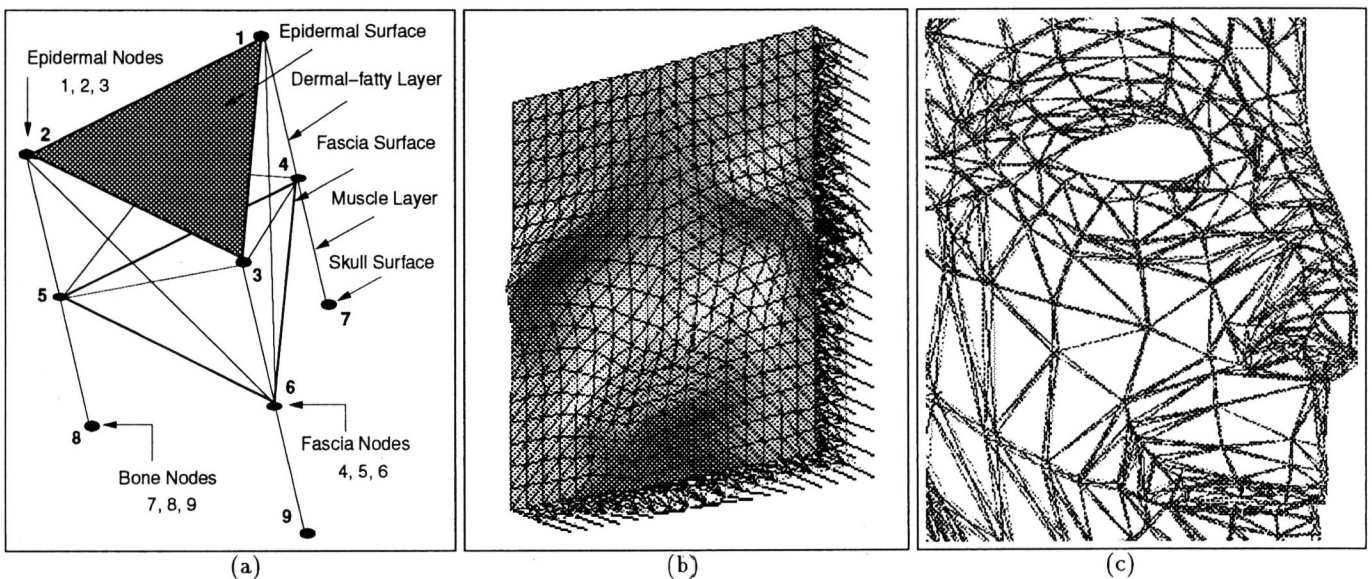


Figure 5: A single facial tissue element (a). Elements assembled as a skin patch with embedded muscles contacted (b). A closer look at half of an adapted face mesh with underlying synthetic tissue (c).

4 Layered Synthetic Tissue Model

From a histologist’s point of view [2], the skull is covered by deformable tissue which has five distinct layers. Four layers—epidermis, dermis, subcutaneous connective tissue, and fascia—comprise the skin, and the fifth consists of the muscles of facial expression. In accordance with the structure of real skin, we have designed a new, synthetic tissue model which is illustrated in Fig. 5.

The tissue model is composed of triangular prism elements like the one shown in Fig. 5(a). The epidermal surface is defined by nodes 1, 2, and 3, which are connected by epidermal springs. The epidermal nodes are also connected by dermal-fatty layer springs to nodes 4, 5, and 6, which define the fascia surface. Fascia nodes are interconnected by fascia springs. They are also connected by muscle layer springs to skull surface nodes 7, 8, 9.

Fig. 5(b) shows 342 such skin elements assembled into an extended “skin patch.” Several “muscles” are embedded into the muscle layer of the skin patch and the figure shows the skin deformation due to muscle contraction. Muscles are fixed in “bone” at their point of emergence and are attached to fascia nodes as they run through several tissue elements. Fig. 5(c) shows a close-up view of the right half of the conformed “Heidi” face which consists of 432 elements.

Springs in the different layers have different stress-strain relationships. Furthermore, in order to efficiently approximate the non-linear stress-strain relationship in the dermal-fatty layer tissue (see [5, 3]), the dermal-fatty springs have two linear phases with different spring stiffnesses in dermal-fatty phase 1 and dermal-fatty phase 2 (see [8]). We also include a rapidly growing nonlinear force function to prevent the spring from reversing itself when it is compressed.

The spring stiffness of biphasic dermal-fatty springs is de-



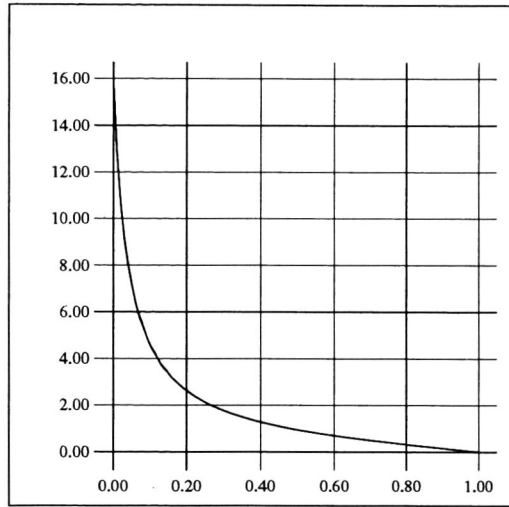


Figure 6: Spring penalty force during compression.

defined as

$$c_s = \begin{cases} I_s K_2 / l_s^r & \text{for } l_s > l_s^r (1 + B_p^s) \\ I_s K_1 / l_s^r & \text{for } l_s^r (1 + B_p^s) > l_s > l_s^r \\ I_s K_1 \Phi(l_s, l_s^r) / l_s^r & \text{for } l_s^r > l_s \end{cases}$$

and the spring stiffness for other springs is

$$c_s = \begin{cases} I_s K / l_s^r & \text{for } l_s > l_s^r \\ I_s K \Phi(l_s, l_s^r) / l_s^r & \text{for } l_s^r > l_s \end{cases}$$

In the above equations, K_1 and K_2 are the two spring stiffnesses for the biphasic dermal-fatty springs, and K is the spring stiffness for other springs. The actual length of spring s is l_s , while l_s^r is its rest length. The spring's biphasic point B_p^s is given in terms of the deformation ratio l_s/l_s^r . The multiplicative factor I_s has value $+1$ when spring s is not inverted, and -1 when inverted. The function $\Phi(l_s, l_s^r) = \tan(\sigma\pi(1 - l_s/l_s^r)/2)$ is the spring compression penalty, where $0 < \sigma < 1$ is a scaling factor. Fig. 6 plots $\Phi(l_s, l_s^r)$ versus the deformation ratio for the default value $\sigma = 0.98$.

The values of the spring stiffness K that we used for springs in the various layers are set as follows:

	Epid	Derm-fat 1	Derm-fat 2	Fascia	Muscle
K	60	30	70	80	10

See [8] for the remaining details on how the spring forces are applied to the tissue nodes.

5 Muscle Forces

The muscles of facial expression, or the muscular plate, spreads out below the facial tissue. The facial musculature attached to the the skin tissue by short elastic tendons at many places in the fascia, but is fixed to the facial skeleton only at a few points. Contractions of the facial muscles cause movement of the facial tissue.

To better emulate the facial muscle attachments to the fascia layer in our model, a group of fascia nodes situated along the muscle path—i.e., within a predetermined distance from a central muscle vector, as determined by the muscle

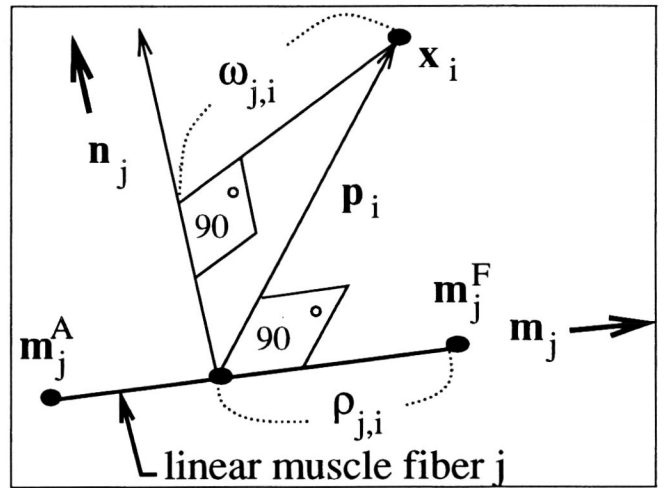


Figure 7: Calculation of muscle force ratios.

width—experience forces from the contraction of the muscle. The face construction algorithm determines the nodes affected by each muscle in a precomputation step. Given a muscle j with fixed node positioned at \mathbf{m}_j^F and attached node at \mathbf{m}_j^A , the algorithm computes the length ratio $\rho_{j,i}$ and width ratio $\omega_{j,i}$ of fascia node i positioned at \mathbf{x}_i in muscle j as follows (see Fig. 7):

$$\begin{aligned} \mathbf{m}_j &= (\mathbf{m}_j^F - \mathbf{m}_j^A) / \|\mathbf{m}_j^F - \mathbf{m}_j^A\| \\ \mathbf{n}_j &= (\mathbf{n}_j^F + \mathbf{n}_j^A) / \|\mathbf{n}_j^F + \mathbf{n}_j^A\| \\ \rho_{j,i} &= (\mathbf{m}_j^F - \mathbf{x}_i) \cdot \mathbf{m}_j \\ \mathbf{p}_i &= \mathbf{x}_i - \mathbf{m}_j^F + \rho_{j,i} \mathbf{m}_j \\ \omega_{j,i} &= \|\mathbf{p}_i - (\mathbf{p}_i \cdot \mathbf{n}_j) \mathbf{n}_j\| \end{aligned}$$

where \mathbf{m}_j is the normalized muscle vector for muscle j , \mathbf{n}_j is the muscle normal which is determined from the nodal normals \mathbf{n}_j^A and \mathbf{n}_j^F of the attached and fixed points of the muscle, and \mathbf{p}_i is the perpendicular vector from \mathbf{m}_j to fascia node i .

The muscle force \mathbf{f}_i^j acting on fascia node i influenced by muscle j is calculated from $\rho_{j,i}$ and $\omega_{j,i}$ as follows (see Fig. 7):

$$\begin{aligned} \epsilon_{j,i} &= \rho_{j,i} / \|\mathbf{m}_j^A - \mathbf{m}_j^F\| \\ \Theta_1(\epsilon_{j,i}) &= \sin(\pi \epsilon_{j,i}^\kappa / 2) + \frac{1}{8} (\sin(2\pi \epsilon_{j,i}^\kappa - \pi/2) + 1) \\ \Theta_2(\omega_{j,i}) &= \frac{1}{2} (\cos(\pi(\omega_{j,i}/w_j)^{1.8}) + 1) \\ \mathbf{f}_i^j &= \Theta_1(\epsilon_{j,i}) \Theta_2(\omega_{j,i}) \mathbf{m}_j \end{aligned}$$

where $0 \leq \epsilon_{j,i} \leq 1$ is the muscle range ratio in length of fascia node i with respect to muscle fiber j . The exponent κ of $\epsilon_{j,i}$ emphasizes the muscle force. When κ is increased beyond unity, the influence of the sine weighting function narrows, and it widens as κ is decreased below unity. The default value is $\kappa = 0.48$. Function Θ_1 scales the muscle force according to the length ratio, while Θ_2 scales it according to the width ratio, where w_j is the muscle width for muscle j . Fig. 8 plots the muscle force \mathbf{f}_i^j with respect to $\epsilon_{j,i}$. Fig. 5(b) shows an example of the effect of muscle forces applied to a synthetic skin patch.



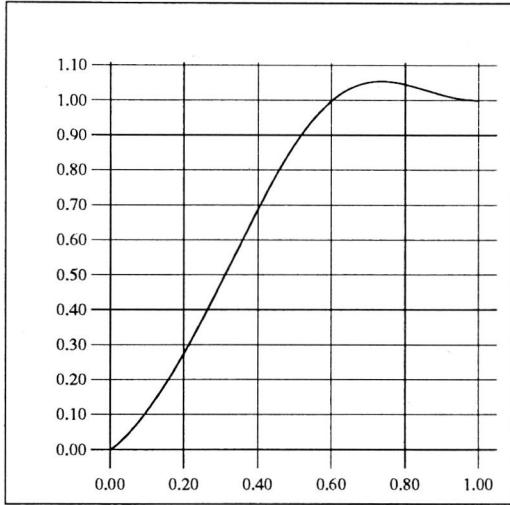


Figure 8: Muscle force profile versus muscle length ratio.

Fig. 9 shows the 26 muscle vectors that we incorporate into our facial model. The number of nodes affected by each muscle—Zygomatic Major, Anguli Depressor, Inner Frontalis, Major Frontalis, Outer Frontalis, Levator Labii, Levator Labii Nasi, Lateral Corrugator, Corrugator, Depressor Labii, Zygomatic Minor, Buccinator, and Mentalis—is as follows:

Muscle	ZygMaj	AngDep	InnFro	MajFro
Width	0.6	0.8	1.2	1.0
Bundles	12	12	12	13

OutFro	LevLab	LevLNa	LatCor	Corrug
1.0	0.3	0.2	0.2	0.4
10	4	4	5	5

DepLab	ZygMin	Buccin	Mental
0.7	0.4	0.8	0.6
16	11	12	21

The attachments of these muscles to skull and fascia are described in [9].

6 Volume Preservation Forces

Facial tissue is primarily water-based, hence it preserves its volume under deformation. As in [8], we add a volume constraint to our spring-mass model which minimizes the volume change by applying an additional force to each epidermal node according to the deformation of the element to which it belongs. For example, in Fig. 5(b), the skin is stretched along the positive x , negative x , and negative y directions. The volume constraint causes it to bulge near the end of the muscles and depress near the central stretching area.

The volume V^e and the volume constraint force \mathbf{q}_i^e at epidermal node $i = 1, 2, 3$ of the prism element defined by nodes 1 to 6 in Fig. 5(a), is calculated as follows:

$$\begin{aligned}
 V_1^e &= (\mathbf{v}_{12}^e \times \mathbf{v}_{13}^e) \cdot \mathbf{v}_{14}^e \\
 V_2^e &= (\mathbf{v}_{65}^e \times \mathbf{v}_{64}^e) \cdot \mathbf{v}_{63}^e \\
 V_3^e &= (\mathbf{v}_{54}^e \times \mathbf{v}_{53}^e) \cdot \mathbf{v}_{52}^e \\
 V^e &= V_1^e + V_2^e + V_3^e \\
 \mathbf{q}_i^e &= k_1(V^e - \tilde{V}^e)\mathbf{n}_i^e + k_2(\mathbf{p}_i^e - \tilde{\mathbf{p}}_i^e)
 \end{aligned}$$

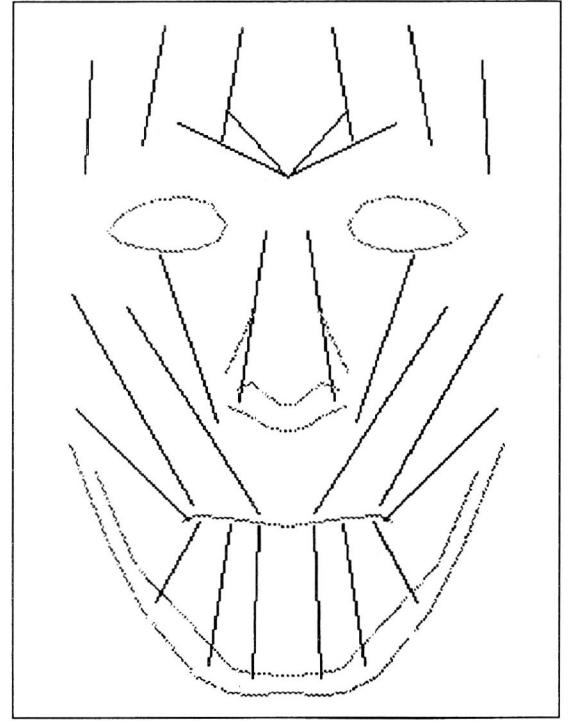


Figure 9: Facial expression muscles relative to generic mesh.

where V_1^e, V_2^e , and V_3^e are the volumes of the three tetrahedra comprising the prism element e , \mathbf{v}_{ij}^e are vectors from node i to node j of e , V^e is the volume of e , \tilde{V}^e is the volume of e in the rest state, \mathbf{n}_i^e is the epidermal normal for epidermal node i , \mathbf{p}_i^e is the nodal coordinate for node i with respect to the center of mass of e , $\tilde{\mathbf{p}}_i^e$ is \mathbf{p}_i^e in the element rest state, and k_1, k_2 are force scaling constants.

7 Skull Penetration Constraint Forces

During a facial expression, the facial muscles slide over the skull and the fascia nodes should not penetrate the skull. To prevent penetration, we compute constraint forces based on estimated skull normals. We estimate the skull normals from the epidermal node normals. In the case of cylindrical data, we directly calculate the normals of the face nodes in cylindrical coordinates and then transform them to generic mesh coordinates. The array of normals to the topographical range map (Fig. 1(a)) is given by

$$\mathbf{n}_{k,l}^c = [(\mathbf{r}_{k+1,l} - \mathbf{r}_{k,l}), 0, 0]^T \times [0, (\mathbf{r}_{k,l+1} - \mathbf{r}_{k,l}), 0]^T$$

where $r_{k,l}$ is the range value at longitude k and latitude l . In certain places, range data is missing. We therefore estimate missing epidermal range values and node normals using interpolation.

The normal vector at node i in the face model is given by (see, e.g., [3])

$$\mathbf{n}_i = \begin{bmatrix} \cos \theta_i & 0 & -\sin \theta_i \\ 0 & 1 & 0 \\ \sin \theta_i & 0 & \cos \theta_i \end{bmatrix} \mathbf{n}_i^c$$

where \mathbf{n}_i^c is the topographic normal of the node computed by interpolation from the array of normals. The angle θ_i in the



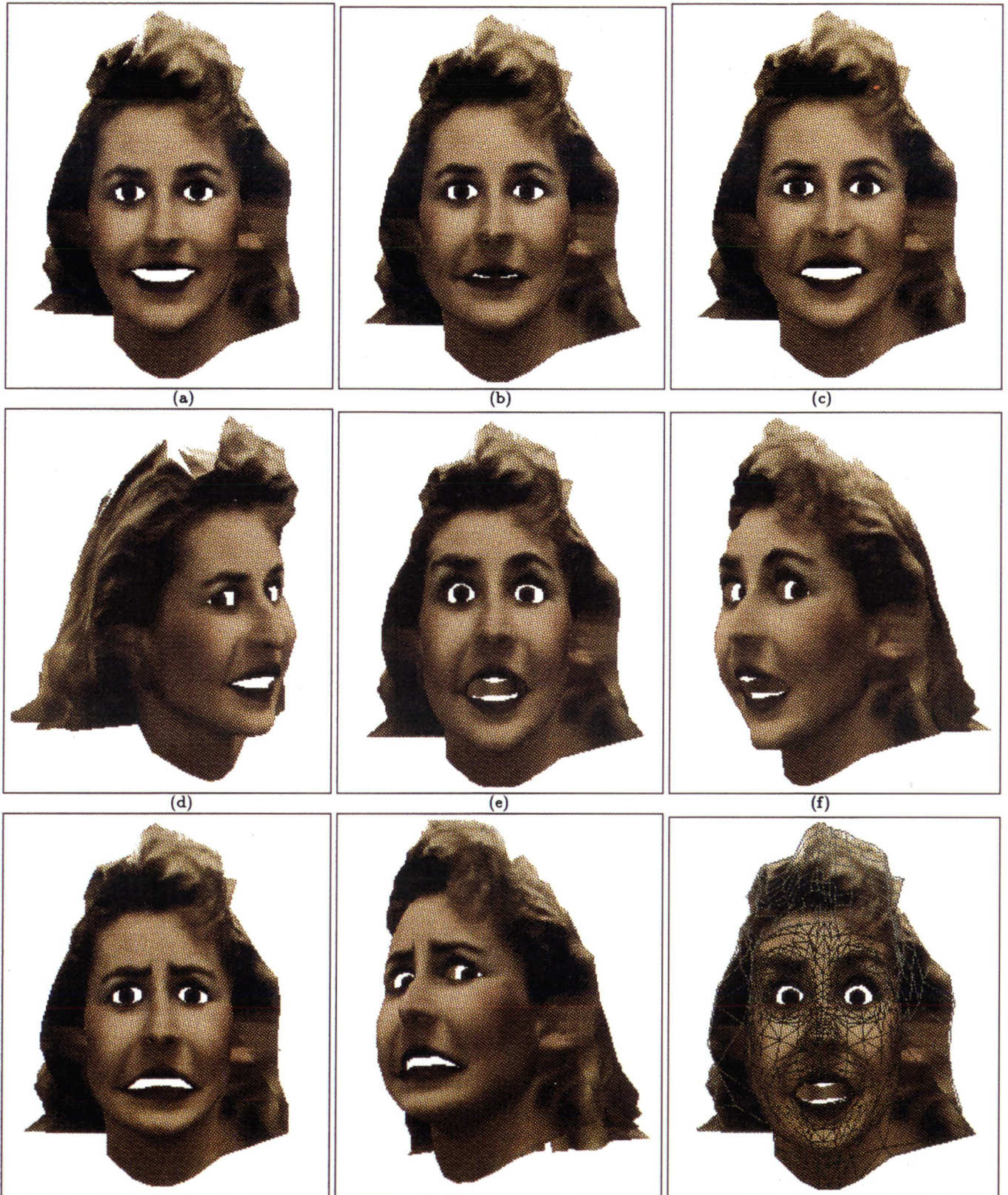


Figure 10: Physics-based head model constructed from "heidi" data set (a). Relaxed face estimated from smiling heidi data (b). Face with contracted zygomatic major, zygomatic minor, depressor labii, and mentalis (c). Side view (d). Face with contracted inner, major, and outer frontalis, and opened jaw (e). Side view (f). Face with contracted inner frontalis, lateral corrugator, anguli depressor, and depressor labii (g). Side view (h). Face in (e) with epidermal superimposed mesh (i).



direction cosines transformation matrix is the rotation angle of node i based on the center of the nose in the positive z direction. For example, for a node with $\theta_i = \pi/2$, which is very close to the left ear, and $\mathbf{n}_i^c = [0, 0, 1]^T$ pointing in the positive z direction in the cylindrical coordinate system will yield an $\mathbf{n}_i = [1, 0, 0]^T$, pointing in the positive x direction.

The forces which prevent the tissue from penetrating the skull surface are

$$\mathbf{s}_i = \begin{cases} -(\mathbf{f}_i^n \cdot \mathbf{n}_i)\mathbf{n}_i & \text{when } \mathbf{f}_i^n \cdot \mathbf{n}_i < 0 \\ \mathbf{0} & \text{otherwise} \end{cases}$$

where \mathbf{f}_i^n is the net force on fascia nodes i .

8 Numerical Simulation

The discrete Lagrange equations of motion for each node i are

$$m_i \frac{d^2 \mathbf{x}_i}{dt^2} + \gamma_i \frac{d\mathbf{x}_i}{dt} + \mathbf{g}_i + \mathbf{q}_i + \mathbf{s}_i + \mathbf{h}_i = \mathbf{f}_i$$

where \mathbf{g}_i is the net spring force, \mathbf{q}_i is the net volume restoration force, \mathbf{s}_i is the skull non-penetration force for fascia nodes, \mathbf{h}_i is a force that restores node i to its rest position, and \mathbf{f}_i is the net muscle driving force acting on node i . The quantity $\gamma_i(d\mathbf{x}_i/dt)$ is a velocity-dependent damping force (see [3]).

As in [8], we use the explicit forward Euler method to perform the integration over time:

$$\begin{aligned} \mathbf{a}_i^t &= \frac{1}{m_i}(\mathbf{f}_i^t - \gamma_i \mathbf{v}_i^t - \mathbf{g}_i^t - \mathbf{q}_i^t - \mathbf{s}_i^t - \mathbf{h}_i^t) \\ \mathbf{v}_i^{t+\Delta t} &= \mathbf{v}_i^t + \Delta t \mathbf{a}_i^t \\ \mathbf{x}_i^{t+\Delta t} &= \mathbf{x}_i^t + \Delta t \mathbf{v}_i^{t+\Delta t} \end{aligned}$$

where \mathbf{a}_i^t , \mathbf{v}_i^t , \mathbf{x}_i^t are the nodal acceleration, velocity, and position of node i at time t , and Δt is the time step.

9 Animation Examples

Fig. 10(a) illustrates several examples of animating the physics-based face model after conformation to the "Heidi" data. Note that Heidi was smiling while she was being scanned, and Figs. 10(a) shows the texture-mapped model conformed to the scanned data. Note that the eyes and teeth are geometric primitives positioned appropriately relative to the skull (cf. [11] in which the eyes and teeth were mapped textures that deformed as the facial tissue deformed!). As we adapt the generic mesh to the smiling face, we also estimate the closed-mouth position so that we can relax the face into the neutral expression shown in 10(b) with relaxed facial muscles.

To generate the "happiness" expression in Figs. 10(c) and 10(d), we contract the Zygomatic Major, Zygomatic Minor Depressor Labii, and Mentalis.

To generate the "surprise" expression in Figs. 10(e) and 10(f), we contract the Frontalis Major, Frontalis Inner, and Frontalis Outer for the upper half of the face, and we open the jaw by rotating the corresponding jawbone skull-nodes of our face model. Fig. 10(i) shows the face in (e) with the epidermal layer mesh superimposed.

To generate the "worry" expression in Fig. 10(g) and 10(h), we contract the Lateral Corrugator and Frontalis Inner, for the upper half of the face, and the Anguli Depressor and Depressor Labii.

10 Conclusion

The human face consists of a biological tissue layer with variable thickness and nonlinear deformation properties, a muscle layer knit together under the skin, and an impenetrable skull structure beneath the muscle layer. This paper has developed a physics-based model of the face which takes all of these structures into account. We have demonstrated a new technique for automatically constructing face models of this sort and conforming them to individuals by exploiting high-resolution laser scanned data. The conformation process is carried out by a feature matching algorithm based on a reusable generic mesh. The conformation process also estimates the skull structure over which the new synthetic facial tissue model can slide. Our facial modeling approach demonstrates an unprecedented level of realism and fidelity to any specific individual.

References

- [1] Cyberware Laboratory, Inc. *4020/RGB 3D Scanner with Color Digitizer*. Monterey, CA, 1990.
- [2] Frick and Hans. *Human Anatomy*, volume 1. Thieme Medical Publishers, Stuttgart, 1991.
- [3] Y. Fung. *A First Course in Continuum Mechanics*. Prentice-Hall, Englewood Cliffs, NJ, 1977.
- [4] M. Hahas, H. Hutric, M. Rioux, and J. Domey. Facial image synthesis using skin texture recording. *Visual Computer*, 6:337-343, 1990.
- [5] W. Larrabee. A finite element model of skin deformation I. biomechanics of skin and soft tissue: a review. *Laryngoscope*, 96:399-405, 1986.
- [6] F. Parke and et al. *State of the Art In Facial Animation*, volume 26, SIGGRAPH'90 Course Notes. ACM SIGGRAPH, 1990.
- [7] D. Terzopoulos and M. Vasilescu. Sampling and reconstruction with adaptive meshes. In *Proceedings of Computer Vision and Pattern Recognition Conference*, pages 70-75. IEEE, June 1991.
- [8] D. Terzopoulos and K. Waters. Physically-based facial modeling, analysis, and animation. *Visualization and Computer Animation*, 1:73-80, 1990.
- [9] J. Warfel. *The Head, Neck, and Trunk*. Lea & Febiger, Philadelphia, PA, 1985.
- [10] K. Waters. A muscle model for animating three-dimensional facial expression. *Computer Graphics*, 22(4):17-24, 1987.
- [11] K. Waters and D. Terzopoulos. Modeling and animating faces using scanned data. *Visualization and Computer Animation*, 2:123-128, 1991.
- [12] K. Waters and D. Terzopoulos. The computer synthesis of expressive faces. *Phil. Trans. R. Soc. Lond.*, 355(1273):87-93, January 1992.

